Atmosphere–Ocean Variations in the Indo-Pacific Sector during ENSO Episodes

NGAR-CHEUNG LAU AND MARY JO NATH

NOAA/Geophysical Fluid Dynamics Laboratory, Princeton University, Princeton, New Jersey

(Manuscript received 21 December 2001, in final form 10 June 2002)

ABSTRACT

The influences of El Niño–Southern Oscillation (ENSO) events on air–sea interaction in the Indian–western Pacific (IWP) Oceans have been investigated using a general circulation model. Observed monthly sea surface temperature (SST) variations in the deep tropical eastern/central Pacific (DTEP) have been inserted in the lower boundary of this model through the 1950–99 period. At all maritime grid points outside of DTEP, the model atmosphere has been coupled with an oceanic mixed layer model with variable depth. Altogether 16 independent model runs have been conducted.

Composite analysis of selected ENSO episodes illustrates that the prescribed SST anomalies in DTEP affect the surface atmospheric circulation and precipitation patterns in IWP through displacements of the near-equatorial Walker circulation and generation of Rossby wave modes in the subtropics. Such atmospheric responses modulate the surface fluxes as well as the oceanic mixed layer depth, and thereby establish a well-defined SST anomaly pattern in the IWP sector several months after the peak in ENSO forcing in DTEP. In most parts of the IWP region, the net SST tendency induced by atmospheric changes has the same polarity as the local composite SST anomaly, thus indicating that the atmospheric forcing acts to reinforce the underlying SST signal.

By analyzing the output from a suite of auxiliary experiments, it is demonstrated that the SST perturbations in IWP (which are primarily generated by ENSO-related atmospheric changes) can, in turn, exert notable influences on the atmospheric conditions over that region. This feedback mechanism also plays an important role in the eastward migration of the subtropical anticyclones over the western Pacific in both hemispheres.

1. Introduction

The widespread influences of the El Niño–Southern Oscillation (ENSO) phenomenon on the global climate system have been documented in numerous observational studies. ENSO-related variations over the Indo-Pacific basin and the surrounding land areas are of particular interest, since both the largest population centers and the most energetic monsoon circulation systems of the world are located in that region. It has been demonstrated that ENSO occurrences are correlated with the intensity of the monsoons over India (e.g., Rasmusson and Carpenter 1983; Mooley and Parthasarathy 1983), east Asia (Zhang et al. 1996), and Australia (McBride and Nicholls 1983). Statistical analyses of historical sea surface temperature (SST) records by many investigators (e.g., Pan and Oort 1983, 1990; Kiladis and Diaz 1989; Nitta and Yamada 1989; Hastenrath et al. 1993; Kawamura 1994; Tourre and White 1995; Lanzante 1996; Nicholson 1997; Harrison and Larkin 1998; Klein et al. 1999; Enfield and Mestas-Nuñez 1999; Larkin and Harrison 2001) have indicated that the surface conditions of the Indian and western Pacific Oceans (hereafter referred to as IWP) are also related to ENSO events. Some of these studies reported that the strongest SST anomalies in IWP typically appear several months after the mature phase of the ENSO signal in the central equatorial Pacific.

One possible interpretation of the observational results cited above is that the rainfall and atmospheric circulation anomalies in the IWP region are primarily remote responses to ENSO forcing in the central and eastern tropical Pacific. These atmospheric perturbations, in turn, influence the underlying ocean through modulation of the surface heat and radiative fluxes, thereby generating SST anomalies in IWP. This chain of processes, hence, play the role of a ''tropical atmospheric bridge'' linking the SST changes in the eastern equatorial Pacific with those in IWP (Klein et al. 1999; Alexander et al. 2002).

A different mechanism linking variability in the Indian and Pacific Oceans has been proposed by Barnett (1985) and Yasunari (1985, 1987), who provided evidence of a global-scale atmospheric signal traveling eastward from Eurasia and the Indian Ocean toward the equatorial Pacific. The analysis performed by Tourre and White (1995) also reveals the presence of eastward-propagating SST anomalies in the Indian Ocean basin.

The prevalence of anomalous SST and sea surface

Corresponding author address: Dr. Ngar-Cheung Lau, NOAA/Geophysical Fluid Dynamics Laboratory, Princeton University, P.O. Box 308, Princeton, NJ 08542.
E-mail: gl@gfdl.noaa.gov

height patterns with marked east–west contrasts in the tropical Indian Ocean basin has been noted in the observational studies of Webster et al. (1999), Saji et al. (1999), and Rao et al. (2002), among others. These authors proposed that such characteristic patterns and the accompanying wind and rainfall anomalies are essentially an expression of internal coupled atmosphere–ocean dynamics, which could be independent from ENSO. However, other studies (e.g., Xie et al. 2002) suggest that conditions of the South Indian Ocean are affected by both ENSO variations and thermocline processes within that ocean. The relative importance of remote forcing from the Pacific sector and local air–sea interaction in the variability of the Indian Ocean climate system is still being debated within the research community (e.g., Allan et al. 2001; Hastenrath 2002; Baquero-Bernal et al. 2002).

The findings reported by Wang et al. (2000), Chang et al. (2000), and Lau and Wu (2001) indicate that the subtropical western North Pacific is another site of active two-way coupling between SST and atmospheric anomalies. It has been shown in these observational studies that the intensity of the low-level anticyclone in that region is correlated with the ENSO signal in the deep Tropics. This anticyclonic anomaly exerts a strong influence on the SST conditions in the South China and Philippine Seas. The ensuing SST changes, in turn, feed back on the overlying atmospheric circulation, and thus affect the evolution of the subtropical high pressure center.

Different hypotheses on the mechanisms contributing to the relationships between ENSO and atmosphere–ocean variability in the IWP region have been tested using general circulation models (GCMs). Many experiments have been conducted to simulate the responses of the Asian–Australian monsoon system to prescribed tropical Pacific SST anomalies in atmospheric GCMs (e.g., see Lau and Nath 2000, hereafter LN00, for a survey of earlier model studies using this approach). Various facets of the atmospheric bridge mechanism have been investigated by allowing the atmospheric response thus generated to interact with simple models of the surface oceans at selected sites outside the tropical Pacific. The oceanic processes that contribute to variability in the IWP region have also been examined by subjecting ocean models of varying degrees of complexity to temporally evolving heat fluxes and wind stresses at the air–sea interface (e.g., Murtugudde and Busalacchi 1999; Behera et al. 2000; Kawamura et al. 2001a,b).

The results in LN00 illustrate that the GCM developed at the Geophysical Fluid Dynamics Laboratory is capable of simulating the broadscale climatological features in the IWP region, as well as reproducing many of the observed relationships between ENSO occurrences and monsoon variations in India, east Asia, and Australia. It is also shown in LN00 that local coupling of these monsoon anomalies with an oceanic mixed layer model could lead to interesting air–sea feedbacks. The purpose of the present study is to extend the work initiated in LN00, by providing a fuller account of the spatiotemporal development of the atmosphere–ocean system in the IWP region in various phases of the ENSO cycle. We examine in greater detail the contribution of surface flux anomalies associated with the atmospheric bridge mechanism to the formation of SST anomalies in different sites within IWP, as well as the nature of the interactions among these oceanic changes and the local atmospheric environment. Special attention is devoted to the lead–lag relationships between different components of the coupled system, and the seasonal dependence of various signals of interest. We attempt to meet these goals by using a new suite of experiments with more appropriate designs and larger ensemble sizes than those analyzed in LN00. Results pertaining to ENSO influences on the entire IWP region are presented in the current paper. Findings that focus on the modulation of the east Asian monsoon by ENSO are reported in a separate article (Lau et al. 2003, hereafter LNW03).

Details of the new experiments are given in section 2. Model and observational results on the covariability of SST fields in the Indo-Pacific basin and the tropical eastern Pacific are displayed in section 3. The typical evolution of atmospheric and SST anomalies in the IWP region through different phases of the ENSO cycle is examined in section 4. The implications of the atmospheric changes on the local surface fluxes and mixed layer depth, as well as the relative contributions of these processes to the local SST tendency, are evaluated in section 5. The local feedbacks between ENSO-induced atmospheric and oceanic changes are further diagnosed in section 6. The findings are summarized and discussed in section 7.

2. Description of model experiments

The experiments analyzed in the present study are based on the same atmospheric GCM as described in LN00. Horizontal variations are represented in this global model using a spectral formulation, with rhomboidal truncation at 30 wavenumbers. Vertical variations are depicted at 14 levels in sigma coordinate. The numerics and physics of this model have mostly been documented in Gordon and Stern (1982) and Broccoli and Manabe (1992). In the present version of the model, the amount of cloud cover is predicted using the scheme described in Wetherald and Manabe (1988). Essential characteristics of the model climatology for the IWP and east Asian regions are described in LN00 and LNW03, respectively.

Two SST scenarios have been incorporated in the GCM integrations for this study. In both scenarios, SST observations for each month within the 50-yr period from 1950 to 1999, as analyzed using the method outlined in Smith et al. (1996), were fed sequentially to the domain situated between 15°S and 15°N, and from

172°E to the South American coast. We shall henceforth refer to this region of SST prescription as the deep tropical eastern/central Pacific (DTEP). The SST conditions outside of DTEP are determined differently in the two scenarios, as follows.

a. The mixed layer model (MLM) experiment

The SST changes at all ice-free maritime grid points beyond the DTEP region have been predicted by coupling the atmospheric GCM to an ocean mixed layer model at those locations. The design of the 31-layer mixed layer model follows that of Gaspar (1988). The incorporation of this mixed layer model in the framework of the atmospheric GCM has been described by Alexander et al. (2000). Based on the energy fluxes, precipitation, and wind stress at each grid point, this model evaluates the local variations in temperature, salinity, and thickness of the mixed layer. No interaction exists between the mixed layer model at neighboring grid points. The flux correction algorithm devised by Manabe et al. (1991) has been implemented, so that the mixed layer model yields a realistic SST climatology. The 50-yr integrations have been repeated 16 times, using distinct initial atmospheric conditions for each member of the ensemble.

b. The control (CTRL) experiment

For every year in the 1950–99 period, the seasonal SST climatology has been imposed at all grid points outside of DTEP. The SST climatology used in this prescription procedure is based on averages of the output from the MLM runs. Application of the MLM climatology to the CTRL runs guarantees that the averaged SST conditions in both experiments are exactly the same, thereby removing the possibility that differences between the two experiments are due to differences in the mean SST forcing outside of DTEP. By virtue of the flux adjustment procedure, the SST climatology of the MLM experiment is very close to its observational counterpart. An ensemble of eight independent integrations has been completed using this design.

The experimental setup for the MLM and CTRL runs bears some correspondence to that of the analogous experiments examined in LN00. The most noteworthy distinctions between the model runs in LN00 and the new experiments are the following:

- Both the longitudinal and latitudinal extents of the region of variable SST prescription in the runs described in LN00 (i.e., entire length of tropical Pacific and 25°S–25°N) are relatively broader. Confinement of this forcing region to grid points east of 172°E in the new experiment allows for the incorporation of air–sea coupling over the tropical western Pacific.
- The single-slab mixed layer with a constant 50-m depth in the LN00 study has been replaced by a multilayer model that explicitly computes variations of the mixed layer thickness. Hence, the new model offers a more realistic representation of the seasonal evolution and interannual variability of the thermal capacity of the surface ocean.
- The number of independent samples for the MLM and CTRL experiments (16 and 8, respectively) is considerably larger than that examined in LN00 (4 each).

TABLE 1. Temporal correlation between the expansion coefficients of the left and right fields (r), and fraction of spatially integrated variance (vf) of the left field explained by time series for the right field, for various lags of the left field relative to the right field. All r and vf statistics (expressed in %) are based on the leading SVD mode for the MLM data.

	Time lag (months)					
	0	1	2	3	4	5
r	79	85	88	90	90	89
vf	20	24	27	29	29	28

In addition to the MLM and CTRL runs, several supplementary experiments have been performed by subjecting the same GCM to temporally fixed SST forcing in the IWP region. The design of the latter integrations and the results derived therefrom are described in section 6b.

3. Covariability of SST in the DTEP and IWP regions

The spatial and temporal characteristics of the Indo-Pacific SST variations that are related to ENSO forcing in the tropical eastern/central Pacific have been examined using a singular value decomposition (SVD) technique. A detailed description of this analysis tool and the pertinent terminology have been given by Bretherton et al. (1992). In the present application, the left field corresponds to the SST pattern in the Indian and western Pacific sector (40°S–40°N, 30°–172°E), whereas the right field is taken to be the SST data in the DTEP region. The input data consist of monthly SST anomalies for all seasons in the 1950–99 period. The SVD procedure was applied both to the 16-run ensemble mean of the MLM experiment, and to observations. Separate SVD analyses have been performed with the left field lagging the right field by various time periods, ranging in monthly intervals from zero to five months. Some selected statistics for the leading SVD mode of the MLM data are shown in Table 1. These results indicate that, when the left field lags by 3–4 months, the correlation between the expansion coefficients of the left and right fields (r) attains the highest values, and the time series for the right field explains the largest fraction of spatially integrated variance (vf) of the left field. The corresponding values of r and vf based on observational data (not shown) are also largest at temporal lags of 1–3 and 3–4 months, respectively. The heterogeneous regression patterns for the leading SVD mode, which

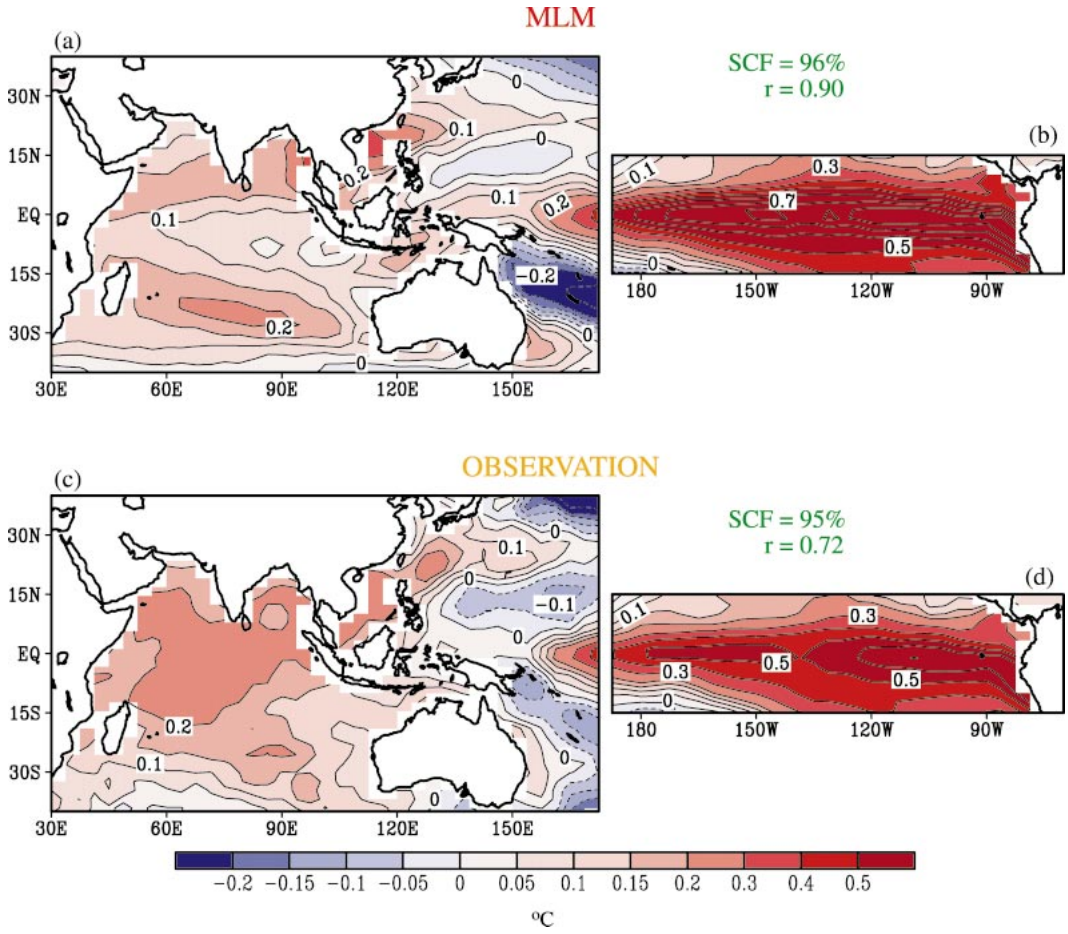

FIG. 1. Heterogeneous regression patterns associated with the leading SVD mode for the SST variations (a), (c) in the IWP (left field) and (b), (d) in the DTEP (right field), as determined on the basis of data for (a), (b) the MLM experiment and (c), (d) observations, and with the left field lagging the right field by four months. Panels (a) and (c) are constructed by regressing SST data at individual grid points in IWP against the time series of standardized expansion coefficients of the right field. Panels (b) and (d) are obtained by regressing SST data in DTEP against the expansion coefficients of the left field. The squared covariance fraction (SCF) explained by the SVD mode and temporal correlation coefficient (r) between the expansion coefficients for the left and right fields are indicated above (b), (d).

show the spatial distributions of the temporal regression coefficients for gridpoint values of the left (right) field versus the standardized expansion time series of the right (left) field, are displayed in Fig. 1 for the MLM experiment (Figs. 1a,b) and observations (Figs. 1c,d). These results are based on the SVD analysis with the left field lagging the right field by four months.

The leading SVD spatial patterns for the MLM experiment illustrate that the zonally elongated SST anomaly near the equator in the DTEP region (Fig. 1b) is typically followed several months later by the occurrence of SST variations of the same polarity in the subtropical northern and southern Indian Ocean, South China Sea, and the waters off the southeastern Australian coast, as well as by SST changes of the opposite sign to the east of the Philippines and along a zone extending southeastward from New Guinea (Fig. 1a). Many of the above relationships between the prescribed forcing in DTEP and the model response in IWP are supported by the corresponding observations (Figs. 1c,d). However, there exist considerable differences between the model and observational results in the equatorial Indian Ocean, where the amplitude of the observed SST anomalies (Fig. 1c) is higher than that in the simulated pattern (Fig. 1a).

Those ENSO events with strong SST signatures in both the DTEP and IWP domains have been identified by inspection of the 50-yr time series of the expansion coefficients for the left and right fields associated with the leading SVD mode of the MLM experiment (not shown). Outstanding episodes have been chosen with the criteria that the amplitudes of the temporal coefficients for both the left and right fields exceed 1.5 standard deviations, and that the maximum amplitudes occur in the northern winter or spring. This selection process yielded the five warm events starting in 1957, 1972, 1982, 1991, and 1997, and the five cold events starting in 1955, 1970, 1973, 1975, and 1988. We shall, hence-

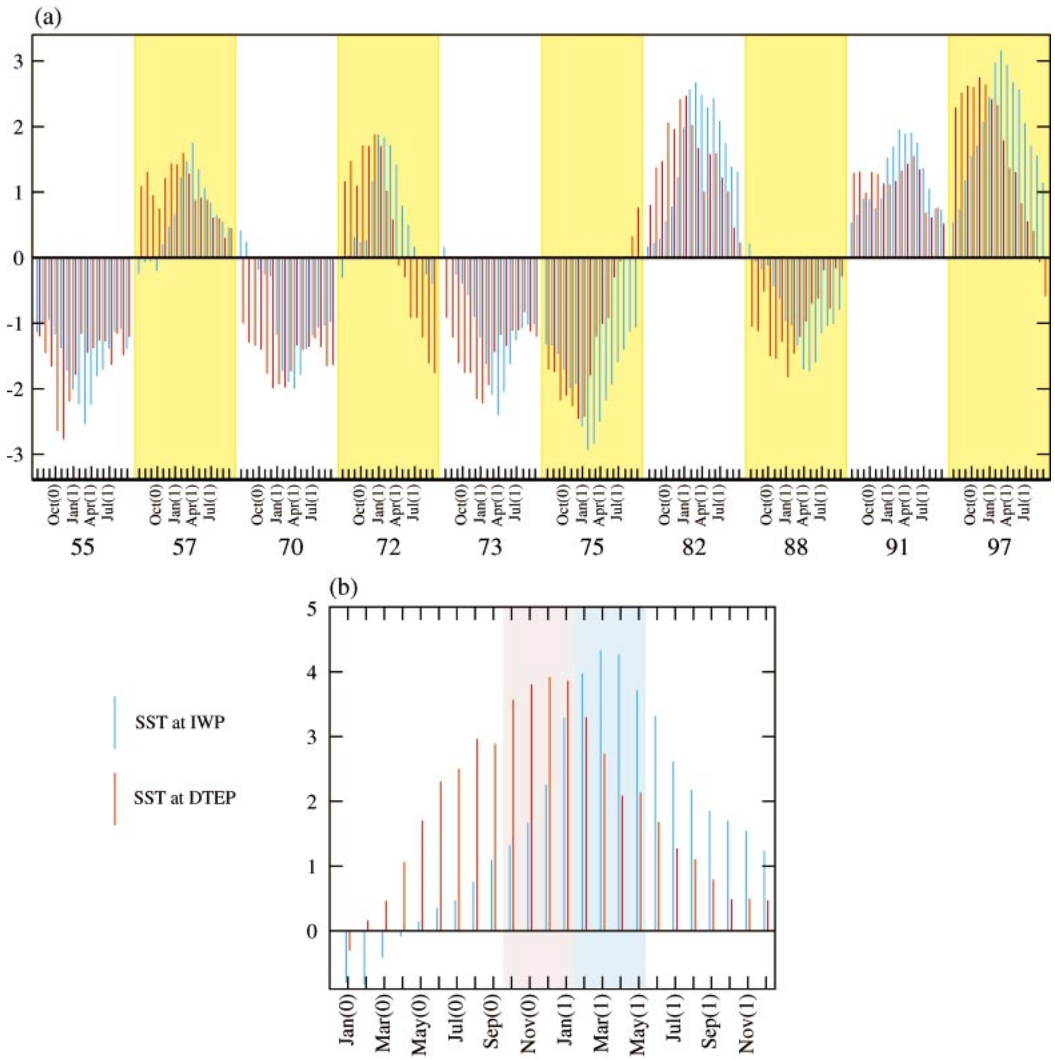

FIG. 2. (a) Time series of the standardized expansion coefficients of the leading SVD mode during the Jul(0)–Oct(1) period of each selected warm and cold ENSO event. (b) Time series of the warm minus cold composite of the expansion coefficients for the left and right fields during years (0) and (1) of the composite episode. All data are based on output from the MLM experiment. The temporal relationships between the left coefficients (blue columns) and right coefficients (red columns) are highlighted by displaying them in juxtaposition in each month. The pink and blue shading in (b) indicate the ONDJ(0/1) and FMAM(1) periods, respectively.

forth, refer to these years as year(0), and the following years as year(1). Specific time periods in the ENSO cycle will be denoted using a three-letter abbreviation of the month, followed by the year indicator in parentheses [e.g., Jan(1) represents the January of year(1)]. The above list of prominent ENSO events is in broad agreement with those compiled by Trenberth (1997) and Wang et al. (2000).

The monthly variations of the standardized expansion coefficients for the leading mode of the MLM experiment within the Jul(0)–Oct(1) period for each of the selected ENSO events are displayed in Fig. 2a. Time series for the right and left fields are depicted with red and blue columns, respectively. This figure shows clearly the 3–4-month lag between the amplitude extrema of the left and right fields during most of the outstanding warm and cold events, with the ENSO forcing in the DTEP region being strongest in the northern winter of year(0/1), followed by peaking of the SST signal in IWP in the spring of year(1). Inspection of the SVD expansion coefficients based on observational SST data (not shown) reveals that, in a majority of the selected warm and cold events, the observed left and right fields exhibit lag relationships and seasonal dependences that are similar to those illustrated in Fig. 2a.

The temporal characteristics of the left and right fields are further illustrated using a composite approach. For each month within the Jan(0)–Dec(1) period and for the left and right fields separately, a ''warm composite'' was obtained by averaging over the expansion coefficients

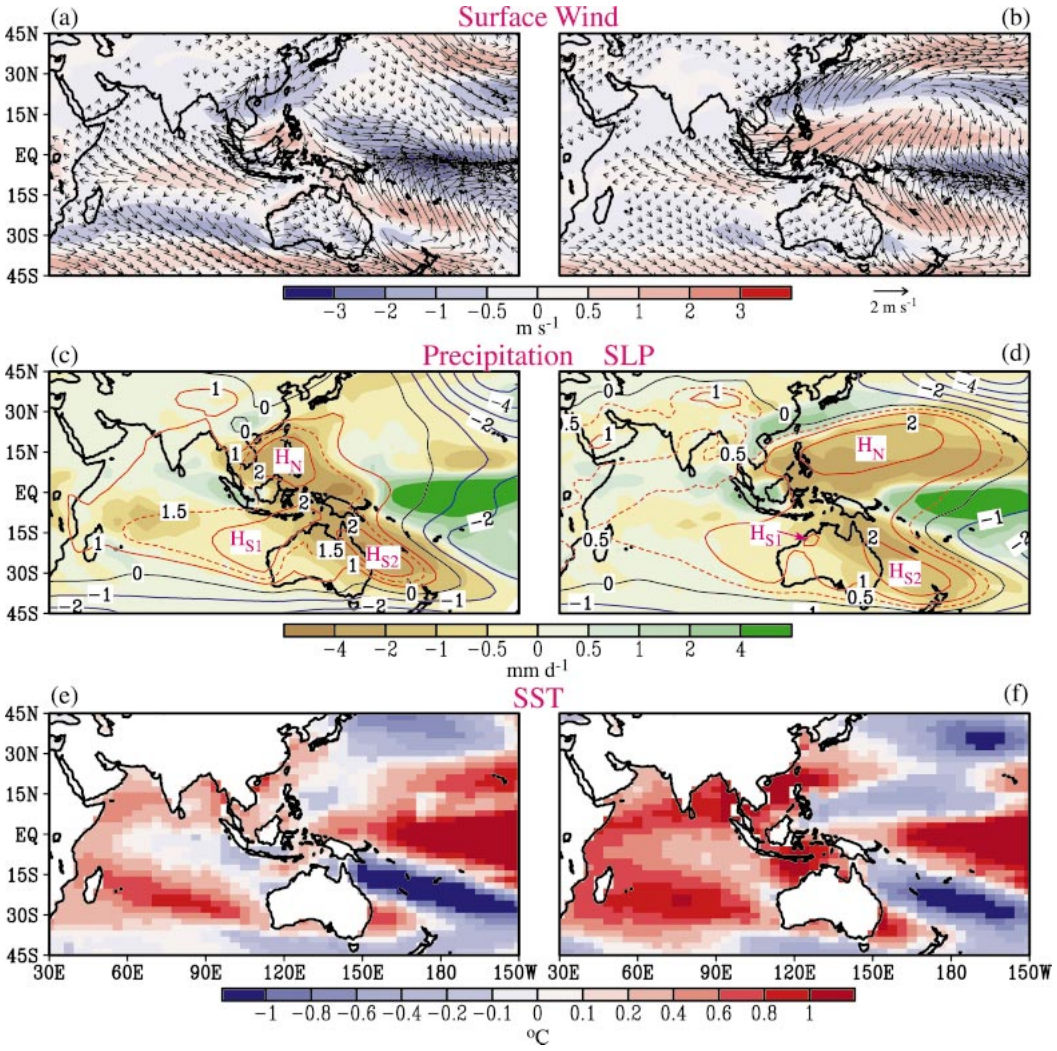

FIG. 3. Distributions of the warm minus cold composites of the (a), (b) surface wind vector (arrows, see scale at bottom right) and surface wind speed (shading); (c), (d) precipitation (shading) and sea level pressure (contours, interval between solid isolines: 1 mb); and (e), (f) SST (shading). Results for the ONDJ(0/1) and FMAM(1) periods are presented in (a), (c), (e) and (b), (d), (f), respectively. All data are based on output from the MLM experiment. The labels H_N, H_{S1}, and H_{S2} in (c), (d) indicate the positions of the anomalous subtropical high pressure centers. In this and following figures, the color scale used for defining the shading in a given panel is shown below that panel.

for the five individual warm events. Similarly, a ''cold composite'' was computed by averaging over the five cold events. Figure 2b shows the temporal variation of the difference between the warm and cold composites (hereafter referred to as the ''warm minus cold composite''). This result confirms the impressions gained from examining the development of individual events in Fig. 2a. The composite time series also provides justification for defining the peak phase of the prescribed forcing in DTEP (right field) as the 4-month period from Oct(0) to Jan(1) [hereafter abbreviated as ONDJ(0/1), indicated by pink shading in Fig. 2b], and the peak phase of the SST pattern in IWP (left field) as the Feb(1)–May(1) period [FMAM(1), light blue shading]. We shall, henceforth, devote our attention to the variations of the coupled system during these two periods.

4. Atmospheric and oceanic changes during peak phases of SST development

The typical characteristics of the simulated atmosphere–ocean system when the SST anomalies in DTEP and IWP attain maximum amplitudes are depicted in Fig. 3, which shows the warm minus cold composites of (Figs. 3a,b) near-surface wind vector (arrows) and wind speed (shading), (Figs. 3c,d) precipitation (shading) and sea level pressure (contours), and (Figs. 3e,f) SST. Data for the ONDJ(0/1) and FMAM(1) periods are

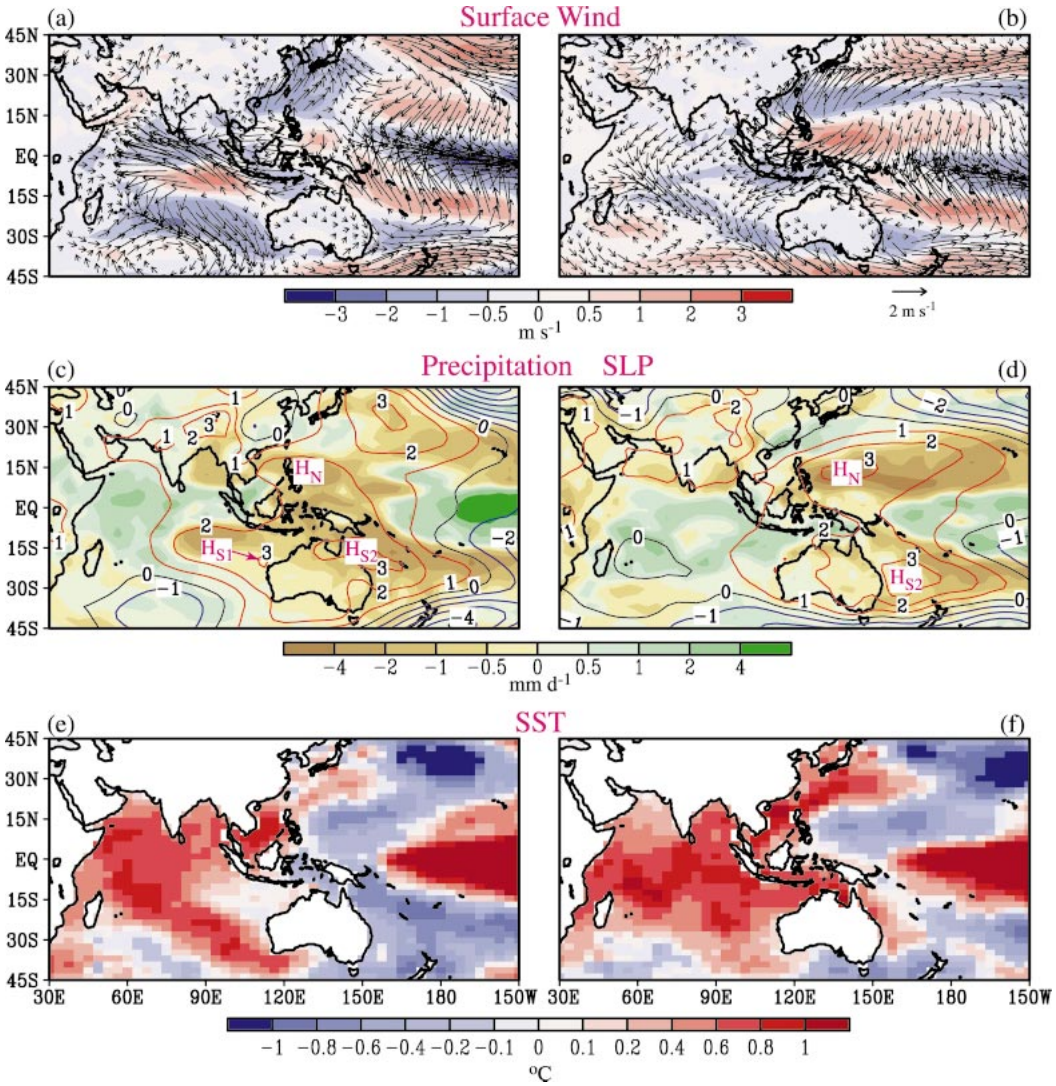

FIG. 4. As in Fig. 3, except for (a)–(d) observational estimates of wind, precipitation, and sea level pressure based on NCEP reanalysis data, and for (e), (f) observed SST data.

plotted in Figs. 3a,c,e and Figs. 3b,d,f, respectively. All results presented in this figure have been obtained using the 16-run ensemble mean of the MLM experiment. The corresponding patterns based on observational estimates provided by the reanalysis and SST products of the National Centers for Environmental Prediction (NCEP) are displayed in Fig. 4. The composite approach adopted here serves to highlight the linear aspects of the atmosphere–ocean responses in IWP to ENSO forcing; that is, Figs. 3–4 portray the linear component of such responses in warm episodes, whereas the corresponding signals in cold episodes would have the opposite polarity. Inspection of the observational and model results for individual warm and cold events does indicate the presence of a linear component in the ENSO-related variations of precipitation (see Figs. 4–5 in LN00 and Fig. 4 in LNW03), zonal wind (Fig. 9 in LN00), and sea level pressure (Fig. 4 in LNW03) at selected sites in the IWP.

It should be stressed that the observed atmospheric and SST anomalies also exhibit significant nonlinearities with respect to the polarity of ENSO. Hoerling et al. (1997) have identified considerable differences in the response patterns of tropical precipitation and midlatitude wave trains in warm and cold events. Asymmetries between the life cycles of atmosphere–ocean phenomena during warm and cold episodes have been documented in detail by Larkin and Harrison (2002). Slingo and Annamalai (2000) further suggested that the monsoon system might reside in distinct circulation regimes depending on the intensity of ENSO events. It is not possible to analyze these nonlinearities using the warm minus cold composite charts presented here. Alternative approaches need to be taken to evaluate the model per-

formance in reproducing the nonlinear responses to ENSO.

a. ONDJ(0/1) period

The simulated atmospheric pattern in the IWP region during the ONDJ(0/1) period of warm events is dominated by a pair of high surface pressure anomalies straddling the equator (Fig. 3c). The northern center (labeled as H_N) is located over the South China Sea and Philippine Sea, and the southern center is most discernible over the eastern Indian Ocean (H_{S1}) and off the northeastern coasts of Australia (H_{S2}). These features correspond closely with the anticyclonic centers identified in Fig. 7d of LN00, and have been attributed to Rossby wave responses to reduced diabatic heating over the equatorial western Pacific in warm ENSO episodes. This interpretation has been substantiated by the results presented by LNW03 (see their Fig. 7). These authors demonstrated that a stationary wave model subjected to anomalous cooling over the tropical western Pacific yields a response that is similar to the sea level pressure pattern in Fig. 3c. The wind pattern in Fig. 3a indicates that H_N is accompanied by a distinct clockwise circulation over Southeast Asia and the subtropical western Pacific; whereas counterclockwise flows related to H_{S1} and H_{S2} are discernible over the subtropical southern Indian Ocean and off the eastern Australian seaboard. Also apparent in Fig. 3a is the divergence of near-equatorial zonal wind anomalies from the Indonesian Archipelago, with prevalent easterlies over the Indian Ocean, and westerlies over the western Pacific. The anomalous flow just north of the equator over the Indian Ocean is mostly directed northward.

The distribution of the changes in surface wind speed (shading in Fig. 3a), which is an important factor for determining heat exchange across the air–sea interface, may be comprehended by comparing the anomalous wind vectors with the climatological flow pattern. Since the mean circulation over the subtropical southern Indian Ocean and off the northeastern Australian coast is oriented from southeast to northwest (e.g., see Fig. 2c of LN00), the southeasterly anomalies on the northern flank of H_{S1} and H_{S2} would enhance the local wind speeds. On the other hand, reduced wind speeds are seen to the south of these anticyclones. Analogously, the anomalous southwesterlies to the north of H_N as well as the anomalous southerlies over the northern Indian Ocean are directed against the climatological winter monsoon.

The anomalous precipitation pattern over the equatorial Pacific (see shading in Fig. 3c) is characterized by enhanced rainfall near the date line and suppressed precipitation within the 120°–150°E zone. These changes are associated with the eastward displacement of the Walker circulation during warm events. Another noteworthy feature in the deep Tropics is the positive rainfall anomaly extending from Sri Lanka to western Indonesia, which is collocated with a convergence zone between northeasterly anomalies over the southern portion of the South China Sea and the southeasterly anomalies over the eastern equatorial Indian Ocean (Fig. 3a). Dryness prevails in the vicinity of the anomalous anticyclones H_N and H_{S2}. Weakening of the dry climatological winter monsoon along the east Asian seaboard leads to above-normal rainfall over southern China.

The SST pattern in Fig. 3e indicates that the mixed layer model generates positive anomalies in the South and East China Seas, the equatorial Pacific just to the west of the region of SST prescription, the waters off the southeastern Australian coast, the 15°–30°S zone in the Indian Ocean, as well as portions of the Bay of Bengal and Arabian Sea. A prominent cold anomaly is simulated along a belt extending southeastward from New Guinea to the southwestern Pacific. The association of this SST feature with the overlying anomalous surface anticyclone (H_{S2}) has previously been noted by Luo and Yamagata (2001). The temperature of the waters to the east of the Philippines and in the eastern equatorial Indian Ocean is also weakly below normal. Many of the SST anomalies in the Indian Ocean and subtropical southwestern Pacific are discernible in the composite patterns for the northern summer of year(0) (not shown). The emergence of these SST signals several months prior to ONDJ(0/1) is associated with the establishment of the anticyclones H_{S1} and H_{S2}, and the weakening of the South Asian monsoon during the Jun(0)–Sep(0) period (see LN00). Comparison between the patterns of SST (Fig. 3e) and wind speed (shading in Fig. 3a) reveals a generally negative spatial relationship between these two fields, with warmer SST occurring where the wind speed is lower than normal, and vice versa. The role of wind speed in modifying the local SST conditions will be examined further in section 5.

b. FMAM(1) period

In the Indian Ocean sector, the composite patterns for the FMAM(1) period (Figs. 3b,d,f) are characterized by considerable weakening of the pressure and wind anomalies as compared to the ONDJ(0/1) period. However, the magnitude of the Indian Ocean SST anomalies in FMAM(1) is comparable to, and in some instances larger than, that in the previous period. Over the western Pacific, the subtropical high pressure centers H_N and H_{S2}, as well as the attendant surface wind and precipitation anomalies, are seen to maintain their individual identities and to migrate eastward with time. For instance, the movement of the center H_N from the Philippines to about 150°E during the two periods is accompanied by a northeastward extension of the enhanced rainbelt over southern China toward Japan (Fig. 3d). The latter finding is suggestive of the intensification of the springtime mei-yu–baiu front over east China during year(1) of warm ENSO events. The SST anomalies east of Australia persist through the two periods

considered here (Figs. 3e,f); whereas the corresponding signals off the east Asian coast exhibit a tendency to travel eastward. The inverse relationship between SST and wind speed anomalies, as noted previously, is also discernible in the western Pacific during the FMAM(1) period.

c. Comparison between model and observations

Many of the above-mentioned model features in both the ONDJ(0/1) and FMAM(1) periods are identifiable in the corresponding patterns based on NCEP observational products (Fig. 4). Particularly noteworthy are the wind and precipitation anomalies organized about the pair of anticyclones on both sides of the equator, the tendency for some of these signals to spread eastward with time, and the attenuation of the sea level pressure anomalies over the Indian Ocean basin from ONDJ(0/1) to FMAM(1). With the exception of the equatorial Indian Ocean, the observational composites support the model inferences on the negative spatial correlation between SST and wind speed changes. The model patterns for surface wind and sea level pressure anomalies in ONDJ(0/1) also bear considerable resemblance to the regression charts presented by Zhang et al. (1997, their Fig. 12) based on an ENSO SST index with interannual timescales.

During the ONDJ(0/1) period, the high pressure center H_N in the model atmosphere is seen to be shifted to the west of its observed position. The composite patterns based on NCEP reanalyses (Figs. 4a,c) indicate the presence of intense anticyclonic flows in the vicinity of a prominent high pressure anomaly centered at 30°N, 160°E; whereas the model results (Figs. 3a,c) show little evidence of these features. The near-equatorial maritime sites between 120° and 160°E are characterized by cold SST anomalies in the observations (Fig. 4e), whereas above-normal SSTs are simulated at the same sites (Fig. 3e).

There are also discrepancies between the observed and modeled wind, precipitation, and SST fields over the Indian Ocean. Of particular note is the prevalence of much stronger observed easterly anomalies along the equatorial belt in that basin during ONDJ(0/1) (Figs. 3a and 4a). The more marked reduction in the observed wind speed in the region between 5°S–10°N and 60°–100°E (Fig. 4a) would result in weakening of the vertical mixing with colder subsurface waters (Venzke et al. 2000). This effect could contribute to the much warmer SST conditions observed in the equatorial Indian Ocean as compared to the model simulation (Figs. 3e,f and 4e,f).

5. Impact of atmospheric variations on air–sea heat exchanges, mixed layer depth, and SST tendency

We now turn our attention to the effects of the atmospheric anomalies discussed in the previous section on the heat fluxes Q at the local air–sea interface and on the thickness of the underlying ocean mixed layer H. We shall also examine how the changes in Q and H affect the local SST field. At a given site, the anomalous time tendency of SST due to fluctuations in Q and H may be expressed as

$$\frac{\partial}{\partial t}\mathrm{SST}' = \frac{1}{\rho C_p}\left(\frac{Q}{H}\right)' = k\left(\frac{Q}{H}\right)', \tag{1}$$

where $k = (\rho C_p)^{-1}$ is assumed to be constant, ρ and C_p are the density and specific heat of ocean water, respectively, and the prime denotes departure from the climatological average. The above expression may be rewritten as

$$\frac{\partial}{\partial t}\mathrm{SST}' = k\frac{Q'}{\overline{H}} + k\overline{Q}\left(\frac{1}{H}\right)', \tag{2}$$

with the two terms on the rhs representing the contributions of anomalies of Q and H to SST changes, respectively. The total surface flux Q can be further decomposed as

$$Q = Q_{\mathrm{SW}} + Q_{\mathrm{LW}} + Q_{\mathrm{LH}} + Q_{\mathrm{SH}}, \tag{3}$$

where Q_{SW} represents the shortwave radiation, Q_{LW} the longwave radiation, Q_{LH} the latent heat flux, and Q_{SH} the sensible heat flux. The sign convention for flux quantities is such that a positive value would result in warming of the ocean mixed layer, and vice versa. In computing Q_{SW}, the shortwave flux penetrating through the base of the ocean mixed layer has been subtracted from the incident flux at the ocean surface. In Fig. 5 are shown the distributions of the warm minus cold composites of the SST tendency due to variations in (Figs. 5a,b) radiative fluxes $k(Q'_{\mathrm{SW}} + Q'_{\mathrm{LW}})/\overline{H}$, (Figs. 5c,d) heat fluxes $k(Q'_{\mathrm{LH}} + Q'_{\mathrm{SH}})/\overline{H}$, and (Figs. 5e,f) mixed layer thickness $k\overline{Q}(1/H)'$. Patterns for the ONDJ(0/1) and FMAM(1) periods are displayed in Figs. 5a,c,e and 5b,d,f, respectively.

a. Surface fluxes

The separate roles of shortwave and longwave fluxes in the SST tendency have been evaluated by examining the individual charts of $kQ'_{\mathrm{SW}}/\overline{H}$ and $kQ'_{\mathrm{LW}}/\overline{H}$ (not shown). These results indicate that the longwave effects tend to oppose the shortwave effects, but that the magnitude of the shortwave fluxes is comparatively larger. Hence the pattern for the net radiative contribution to the SST tendency (Figs. 5a,b) is qualitatively similar to that of $kQ'_{\mathrm{SW}}/\overline{H}$, but with reduced amplitudes. The analysis of the surface flux variations in the IWP region by Klein et al. (1999) using satellite data indicates that the anomalous absorbed shortwave radiation is primarily determined by changes in the local cloud cover. The cloud cover is in turn related to the precipitation field. Comparison between the patterns for radiative effects in Figs. 5a,b and those for precipitation (Figs. 3c,d)

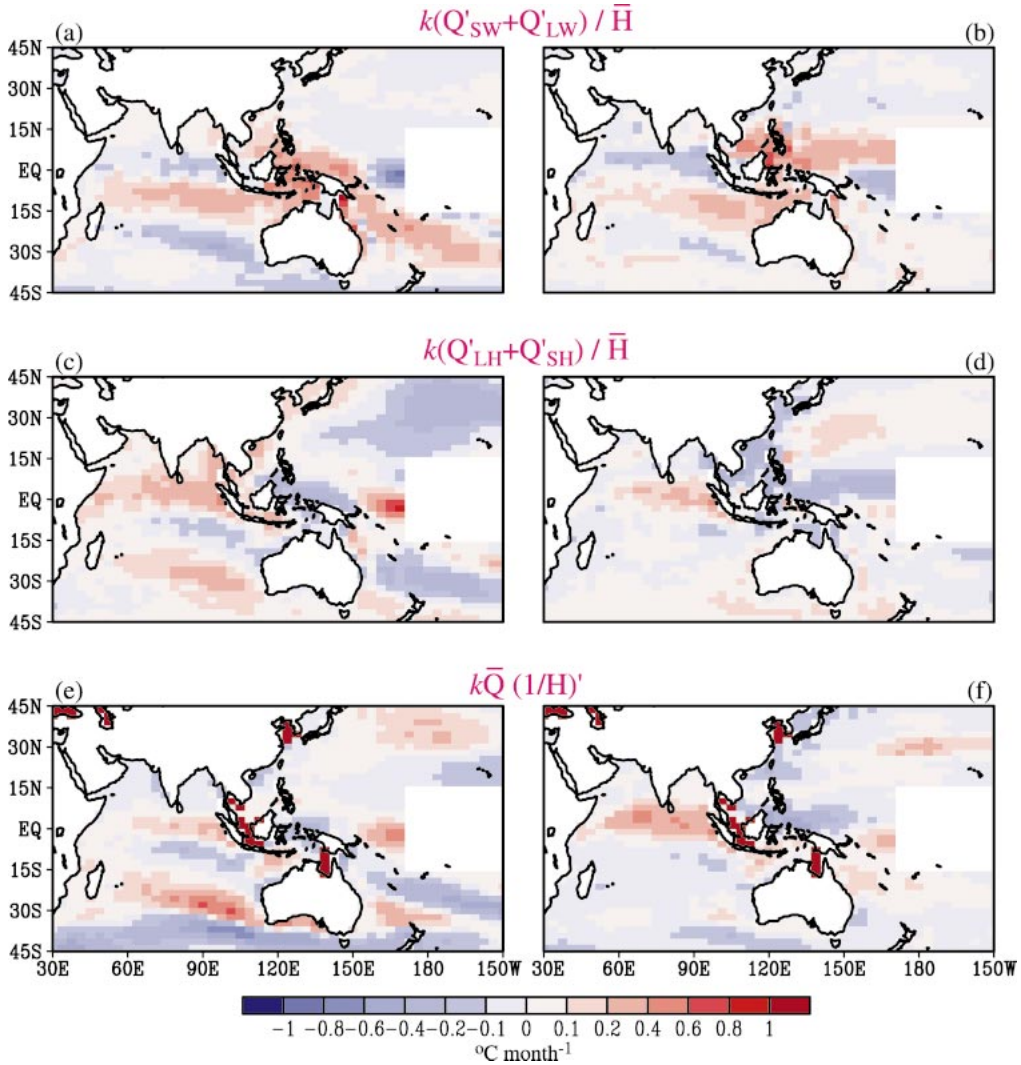

FIG. 5. Distributions of the warm minus cold composites of the SST tendency due to anomalies of (a), (b) shortwave and longwave radiative fluxes; (c), (d) latent and sensible heat fluxes; and (e), (f) mixed layer thickness. See text for definitions of these individual components of the SST budget. Results for the ONDJ(0/1) and FMAM(1) periods are presented in (a), (c), (e) and (b), (d), (f), respectively. All data are based on output from the MLM experiment. Data are not shown in the deep Tropics east of 172°E, where SST forcing has been prescribed. Units: °C month^{-1}.

indicates that the above relationships are simulated in the model. For instance, increased radiative heating of the ocean surface is seen to occur at the dry zones associated with the anomalous subtropical anticyclones in both hemispheres; whereas reduced heating prevails along the enhanced rainbelts in the Indian Ocean just north of the equator. Some similarities exist between the patterns in Figs. 5a,b and the observed distribution of ENSO-related anomalies of incoming solar radiation, as documented by Klein et al. (1999, their Fig. 3c).

Inspection of the composite charts for the individual terms $kQ'_{LH}/\overline{H}$ and $kQ'_{SH}/\overline{H}$ (not shown) indicates that the latent heat flux component makes the dominant contribution to the tropical features in Figs. 5c,d. The intensity and polarity of Q'_{LH} are related to the local wind speed and humidity by the bulk aerodynamic law: strong winds and dry conditions would result in enhanced loss of latent heat to the atmosphere and oceanic cooling, and vice versa. The composite charts for heat flux (Figs. 5c,d) and those for wind speed and rainfall (shading in Figs. 3a–d) are in support of this interpretation. In particular, cooling tendencies due to latent and sensible heat fluxes prevail on the equatorial flanks of the subtropical high centers H_{S1}, H_{S2}, and H_N, where the wind speed is enhanced and precipitation is suppressed. Conversely, positive SST tendencies are generated in the Indian Ocean north of the equator and within the 20°–35°S belt during ONDJ(0/1), which are characterized by lower wind speeds and wet conditions. The simulated SST increases in the South China Sea and northern Indian

Ocean in ONDJ(0/1) due to latent heat fluxes are consistent with the ship measurements analyzed by Klein et al. (1999, their Fig. 7a). The important role of wind-induced variations of latent heat transfer in warming the southern Indian Ocean has been noted in the observational study by Yu and Reinecker (1999).

In view of the opposing effects of precipitation anomalies on Q'_{SW} and Q'_{LH}, as noted in the above paragraphs, there is a discernible negative spatial correlation between the tropical patterns in SST tendencies due to radiative fluxes (Figs. 5a,b) and the corresponding charts for heat fluxes (Figs. 5c,d). It is also worth mentioning that the seasonal variations of the climatological mixed layer thickness $\overline{H}$ (which are particularly pronounced in the subtropics and extratropics) play a critical role in determining the local magnitude of the tendency terms for both radiative and heat fluxes (Figs. 5a–d). For instance, $\overline{H}$ in the 20°–40°S zone of the Indian and western Pacific Oceans increases from ~25 m in the local warm season (ONDJ) to more than 50 m in autumn (FMAM), thus leading to much more prominent signals for the radiative and heat fluxes in the southern oceans in ONDJ(0/1) (Figs. 5a,c) than in FMAM(1) (Figs. 5b,d).

b. Mixed layer depth

The contribution of changes in the mixed layer thickness to the SST tendency is depicted by the patterns for $k\overline{Q}(1/H)'$ in Figs. 5e,f [see definitions in Eqs. (1) and (2)]. For $\overline{Q} > 0$ (i.e., warming by total climatological surface flux), an increase of the mixed layer thickness $[(1/H)' < 0]$ would require that the warming be distributed through a deeper water column, thus leading to a weaker SST tendency than normal. Conversely, reduction in H would result in above-normal SST tendency. The above relationships would be reversed when the climatological fluxes cool the mixed layer ($\overline{Q} < 0$). The modeling study of Murtugudde and Busalacchi (1999) has also demonstrated the dependence of the magnitude of SST anomalies on thermocline depth. The variations of H are governed by entrainment of deep water to the mixed layer, which, in turn, depends upon the intensity of surface wind stirring (see Alexander et al. 2000). Comparison between the composite charts for wind speed (Figs. 3a,b) and mixed layer depth (not shown) confirms that stronger winds are associated with deeper mixed layers, and vice versa.

During the ONDJ(0/1) period, the distribution of $\overline{Q}$ (not shown) is characterized by oceanic warming south of 5°N, and cooling north of that latitude. In accordance with the physical arguments in the preceding paragraph, the pattern for $k\overline{Q}(1/H)'$ (Fig. 5e) and that for wind speed (Fig. 3a) exhibit a strong negative spatial correlation with each other in the near-equatorial and southern oceans, and a positive correlation in regions farther north. During the near-equinoctial period of FMAM(1), $\overline{Q}$ is positive between ~10°S and ~15°N. Hence the anomalies in $k\overline{Q}(1/H)'$ (Fig. 5f) and wind speed (Fig. 3b) tend to have opposite polarities in the deep tropical sites.

There exists a positive spatial correlation between the composite patterns for $k\overline{Q}(1/H)'$ and $k(Q'_{LH} + Q'_{SH})/\overline{H}$ in regions where $\overline{Q} > 0$ (see Figs. 5c–f). This result is consistent with the role of wind speed in modulating both the latent and sensible heat fluxes (through the bulk aerodynamic law) and the mixed layer depth (through entrainment effects).

c. Total SST tendency

To illustrate the net effect of local reinforcements and cancellations among the contributions from different surface flux components and from changes in H, the sum of all three panels in Fig. 5 for each time period has been taken and the results are displayed in Figs. 6a,b. The dominant contribution to the total tendency (Figs. 6a,b) in many tropical sites comes from the cooperative effects of latent and sensible heat fluxes (Figs. 5c,d) and variations of the mixed layer depth (Figs. 5e,f), which more than offset the opposing tendency due to radiative fluxes (Figs. 5a,b).

In addition to the processes considered above, the temperature of the mixed layer is also influenced by several other mechanisms operating below the ocean surface, which include temperature entrainment at the base of the mixed layer, diffusion, and convective mixing (see Alexander et al. 2000 for details). A complete heat budget analysis for the mixed layer is not attempted here. We shall only make a few remarks on these subsurface effects on the basis of composite charts for their individual contributions to the SST tendency (not shown). The magnitude of the diffusion term is small throughout the IWP domain. With the exception of a limited number of grid points in the equatorial western Pacific, the effect of convective mixing is also negligible. The temperature entrainment term is relatively larger in the western edge of the tropical Pacific, where the warm minus cold composite values attain amplitudes of 0.2–0.4°C month^{-1}. Incorporation of this entrainment term in the total SST tendency would alter the pattern of Figs. 6a,b in the equatorial western Pacific somewhat, but would have only minor effects elsewhere.

d. Characteristic timescale of SST development

The total SST tendency shown in Figs. 6a,b exhibits notable spatial relationships with the composite charts for the contemporaneous SST anomalies (Figs. 3e,f). For instance, both Figs. 3e and 6a show positive anomalies in the northern and southern subtropics of the Indian Ocean basin. There is also some resemblance between the composite patterns for tendency and SST in the subtropical southwestern Pacific in ONDJ(0/1). The nature and characteristic timescale for the interactions between the atmospheric forcing (as represented by the

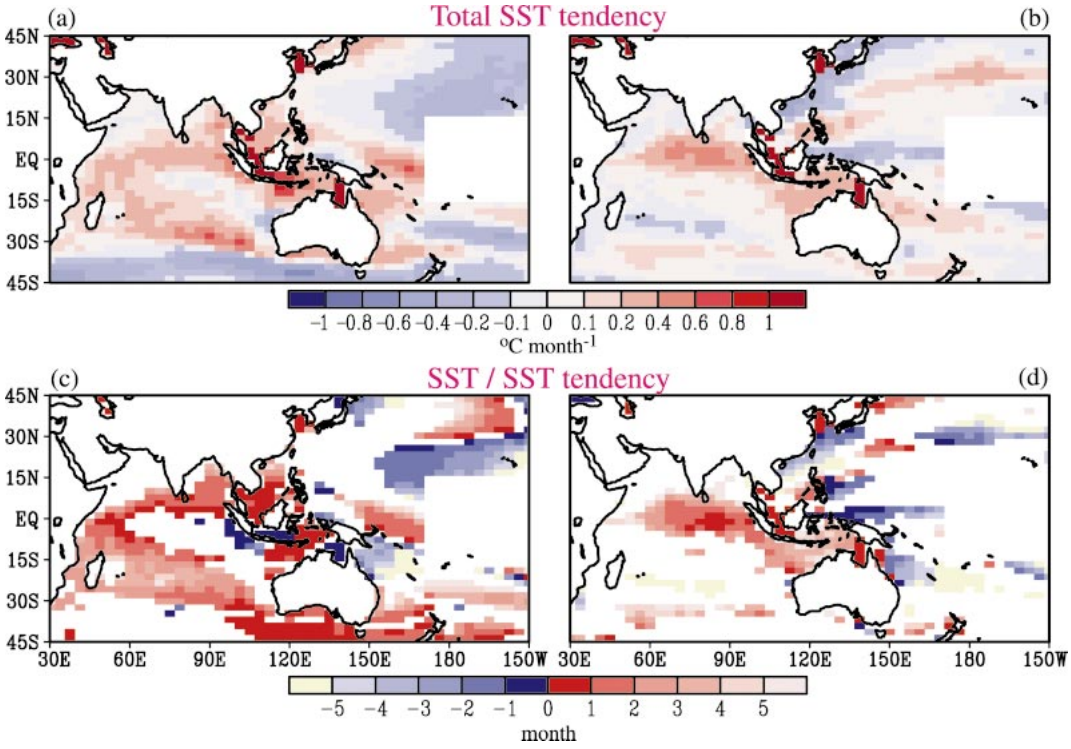

FIG. 6. Distributions of (a), (b) warm minus cold composites of the total SST tendency due to anomalies of radiative fluxes, heat fluxes, and mixed layer depth; units: °C month^{-1}; (c), (d) ratio of the warm minus cold composite of SST anomaly to that of total SST tendency; units: month. The ratio in (c), (d) is shown only at those grid points where the amplitudes of the composite SST anomaly and SST tendency exceed 0.1°C and 0.1°C month^{-1}, respectively. Results for the ONDJ(0/1) and FMAM(1) periods are presented in (a), (c) and (b), (d), respectively. All data are based on output from the MLM experiment. Data are not shown in the deep Tropics east of 172°E, where SST forcing has been prescribed.

total SST tendency term) and the local SST field may be portrayed by the ratio of warm minus cold composite values of SST to those of SST tendency at each grid point, as shown in Figs. 6c,d for the ONDJ(0/1) and FMAM(1) periods. The sign of this ratio indicates whether the atmospheric forcing is conducive to amplification (for positive ratio) or attenuation (for negative ratio) of the local SST anomaly. The magnitude of this ratio (expressed here in units of months) provides a measure of the typical timescale for the composite atmospheric forcing to establish or destroy the composite SST signal. The estimation of this ratio is often unreliable when the numerator and denominator are close to zero. To avoid such situations, values of this ratio are shown only at those grid points where the amplitudes of the composite SST anomaly and SST tendency exceed 0.1°C and 0.1°C month^{-1}, respectively.

The ratio for the ONDJ(0/1) period (Fig. 6c) is positive for a majority of grid points in the Indian Ocean, subtropical southwestern Pacific within the 20°–40°S zone, South China Sea, and the equatorial Pacific between 150°E and the date line, thus indicating the prevalence of SST reinforcement by the overlying atmospheric forcing. The characteristic timescale for this cooperative air–sea interaction is seen to be 1–4 months. The most prominent features in the pattern for FMAM(1) are the positive ratios over the Indian Ocean just north of the equator, as well as off the northwestern Australian coast. The rather noisy distribution over the subtropical northwestern Pacific in this period is primarily due to the near-quadrature spatial relationship between the local SST and tendency fields, as documented in further detail by LNW03. The latter authors also noted that this phase lag may contribute to the salient eastward migration of atmospheric and oceanic signals in that region (see Fig. 3).

6. Feedback of SST anomalies in IWP on the atmosphere

The discussions in the previous sections are primarily concerned with the remote atmospheric response to the SST variations imposed in the DTEP region, and the implications of these atmospheric changes on the surface condition of the oceans in the IWP sector. The SST anomalies that are generated by this atmospheric bridge mechanism could in turn affect the overlying atmosphere. The present section is devoted to the diagnosis of the nature of these air–sea feedbacks.

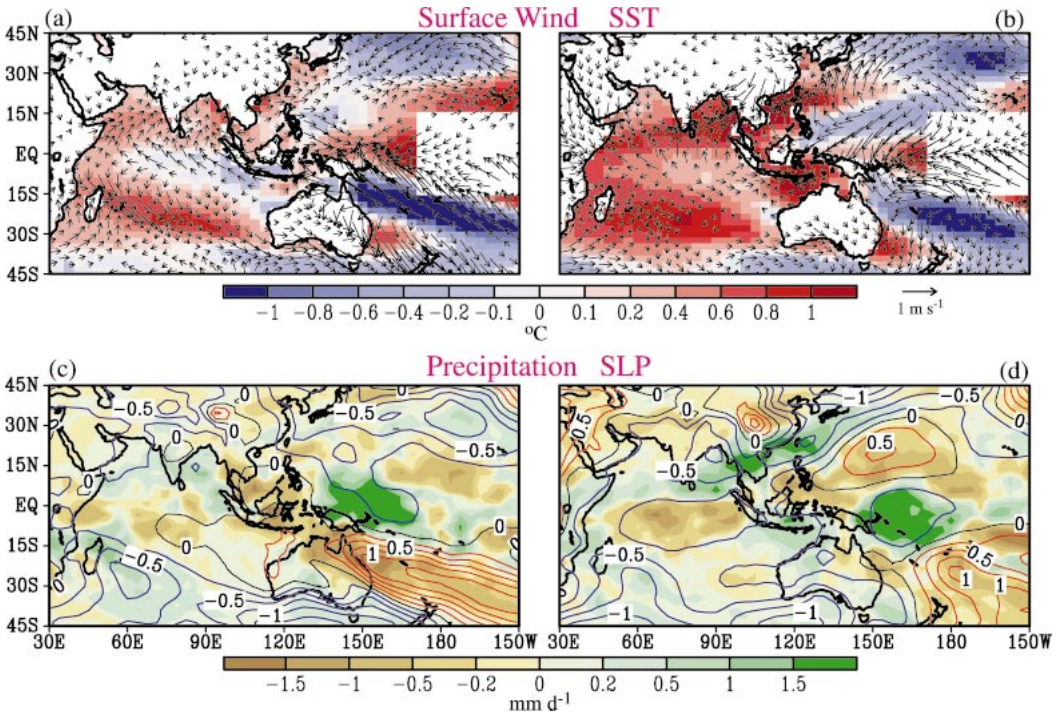

FIG. 7. Distributions of the differences between the MLM and CTRL experiments, as obtained by subtracting the warm minus cold composites based on CTRL output from those based on MLM data, for (a), (b) surface wind vector (arrows, see scale at bottom right) and SST (shading); and (c), (d) precipitation (shading) and sea level pressure (contours, interval: 0.25 mb). Results for the ONDJ(0/1) and FMAM(1) periods are presented in (a), (c) and (b), (d), respectively.

a. Inferences from comparison of MLM and CTRL experiments

The model findings presented thus far are based on the MLM experiment, which incorporates both the prescribed oceanic forcing in DTEP, and the two-way coupling between the ocean mixed layer and the atmosphere outside of that region. As described in section 2, a parallel set of control (CTRL) runs has also been conducted for this study. The latter experiment considers the SST forcing in DTEP only, whereas the air–sea feedbacks elsewhere have been eliminated by fixing the SST conditions at all maritime grid points outside of DTEP at their climatological setting. Hence, the contributions of air–sea interactions to the atmospheric anomalies simulated over IWP may be inferred by taking the differences between the output from the MLM and CTRL experiments.

The warm minus cold composites of selected variables have been computed separately for the MLM and CTRL experiments. Difference charts were then constructed by subtracting the composite data for CTRL from those for MLM. The resulting patterns are shown in Figs. 7a,b for surface wind vectors (arrows) and SST (shading), and Figs. 7c,d for precipitation (shading) and sea level pressure (contours). Results for the ONDJ(0/1) and FMAM(1) periods are displayed in Figs. 7a,c and 7b,d, respectively. Since there is no interannual variability in the SST field beyond DTEP in the CTRL experiment, the warm minus cold composite of this field yields zero values everywhere outside of DTEP. The difference patterns shown here for SST in the IWP region are therefore identical to those of the warm minus cold composites based on the MLM experiment alone (Figs. 3e,f).

1) ONDJ(0/1) PERIOD

The difference chart for surface wind in the Indian Ocean basin during this period (Fig. 7a) is characterized by divergence from the equator, and convergence to the subtropical zones in both hemispheres, where SST warming has been simulated in the MLM experiment. The most notable features in the western Pacific include surface wind convergence over the warm equatorial SST anomaly west of the date line, anticyclonic circulation over the cold anomaly off the northeastern Australian coast, and northeastward flow over the South China and East China Seas. The corresponding chart for precipitation and pressure (Fig. 7c) shows that the convergence east of Madagascar, the Bay of Bengal, and the equatorial western Pacific is accompanied by negative differences (MLM versus CTRL) in surface pressure and positive differences in precipitation. The relatively stronger anticyclonic flow over the subtropical south-

western Pacific in the MLM experiment is collocated with stronger positive pressure and negative precipitation anomalies in that experiment.

The positive precipitation signal over the equatorial western Pacific in Fig. 7c is situated over a warm SST anomaly simulated in MLM (Fig. 7a). As noted in section 4c, the latter SST feature is not discernible in the observational data (see Fig. 4e). These considerations suggest that the precipitation over the equatorial western Pacific may be overestimated in the MLM experiment. This excessive condensational heating generated in the deep Tropics could partially explain the much weaker anticyclonic center near 30°N, 160°E in the MLM composites (Figs. 3a,c) as compared with the observations (Figs. 4a,c).

Over the tropical Indian Ocean and off the Chinese coast, the surface wind vector pattern in the difference chart (Fig. 7a) bears a considerable resemblance to the corresponding composite pattern based on MLM data (Fig. 3a), thus implying that local air–sea coupling contributes to the atmospheric circulation anomaly in that region as simulated in the MLM experiment. Over the subtropical southwestern Pacific, the anticyclonic wind vectors and positive pressure center in the difference chart (Figs. 7a,c) are located to the east of the corresponding features simulated in MLM (Figs. 3a,c). This spatial displacement suggests that air-sea interaction may play a role in the eastward movement of the anomalous anticyclone and high pressure center over the southwestern Pacific (H_{S2}) during the austral summer and autumn of year(0/1) in the MLM experiment (Figs. 3a–d).

2) FMAM(1) PERIOD

The difference chart for wind vectors in this period is characterized by further strengthening of surface convergence along the belt of positive SST anomalies extending northeastward from the Arabian Sea to the Bay of Bengal and the South China Sea (Fig. 7b). Positive precipitation and negative pressure differences prevail in this convergence zone (Fig. 7d). The wind convergence and positive precipitation differences over the equatorial western Pacific, as noted earlier in the ONDJ(0/1) pattern, persist through FMAM(1). The difference pattern over the subtropical northwestern Pacific is dominated in the latter period by an anticyclonic center, where the MLM experiment generates stronger positive pressure and negative precipitation anomalies relative to the CTRL run. In Fig. 7d, the positive pressure difference on the eastern flank of the high anomaly H_N in the MLM experiment (see Fig. 3d) is indicative of the role of air–sea coupling in the eastward development of H_N. A more detailed description of the impact of atmosphere–ocean feedbacks on the spatiotemporal evolution of H_N has been given by Wang et al. (2000) and LNW03.

Comparison between the difference chart and the composite pattern based on the MLM simulation (Figs. 3b,d,f and 7b,d) reveals that the inclusion of atmosphere–ocean feedbacks in MLM leads to reinforcement of the wet anomaly along the mei-yu–baiu front over east Asia during the spring of year(1). A more detailed diagnosis of the variability of this rainbelt over the east Asian seaboard as well as the relative impacts of remote ENSO forcing and in situ air–sea interactions on this feature has been performed by LNW03. It is demonstrated in that study that the composite precipitation and sea level pressure anomalies associated with the mei-yu–baiu front (Figs. 3d and 7d) are discernible in individual warm and cold ENSO events, and in a majority of the 16 independent samples for each event. The signals for individual ENSO episodes are in agreement with the corresponding observational estimates. The results presented in LNW03 also indicate an important role of the SST anomalies in the subtropical northwestern Pacific in modulating the intensity of the mei-yu–baiu front.

b. *Model responses to prescribed SST forcing in IWP*

The evidence presented in the previous section illustrates a strong spatial correspondence between the SST anomalies generated by the MLM experiment in IWP and the difference patterns for various atmospheric fields. For instance, the strength of the convergence and rainfall is relatively stronger in MLM than in CTRL over positive SST anomalies, and vice versa. The nature of these relationships suggests that the meteorological patterns in Fig. 7 primarily result from the feedback of the SST changes in IWP on the overlying atmosphere. We now proceed to test the validity of this interpretation by analyzing the output from an auxiliary set of model experiments. In each 5000-day integration, the solar forcing has been fixed at a particular phase of the seasonal cycle (either mid-January or mid-April). For each of these seasonal settings, two separate runs have been conducted.

- *The climatological (CLIMO) experiment:* Climatological SST conditions for the corresponding phase of the seasonal cycle (i.e., January or April), as obtained from long-term averages of the SST field in the MLM run, have been prescribed at all ocean grid points throughout the course of the integration.
- *The doubled SST anomaly (2 × SST) experiment:* A temporally fixed SST anomaly, as obtained by doubling the warm minus cold composite of the SST data produced in the MLM experiment during the corresponding calendar month in year(1) [i.e., Jan(1) or Apr(1)], has been added to the SST climatology at most of the grid points in the IWP region. The same climatological SST conditions as those used in the CLIMO experiment have been prescribed at grid points lying in the equatorial Pacific and at all sites outside of IWP.

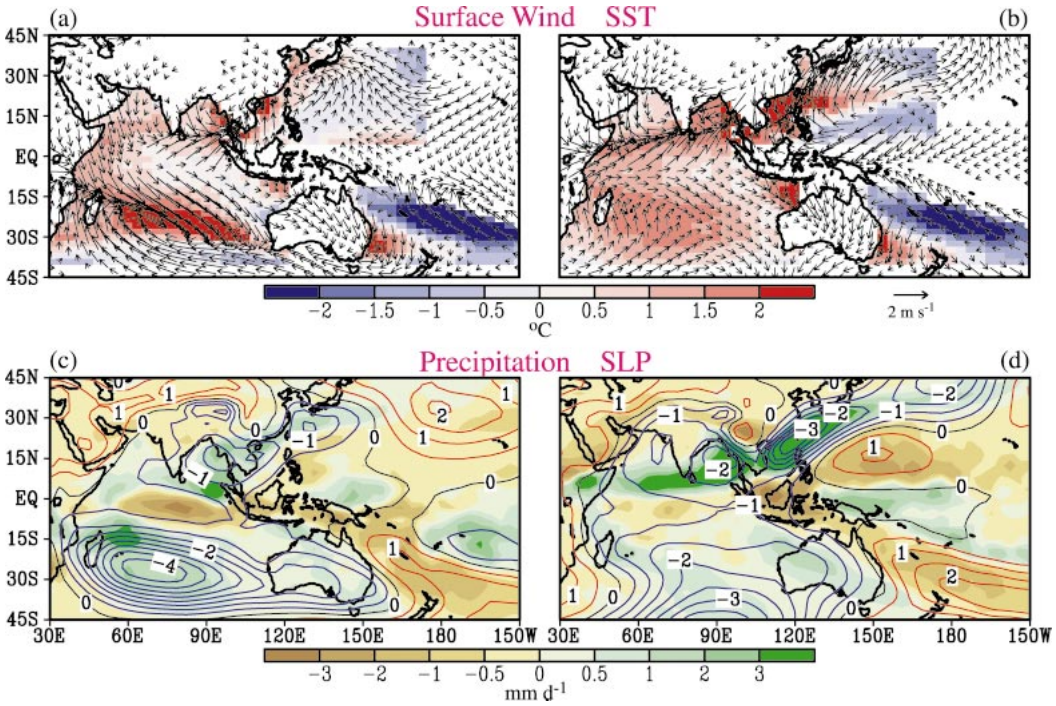

FIG. 8. Distributions of the differences between the 2 × SST and CLIMO experiments, for (a), (b) surface wind vector (arrows, see scale at bottom right) and SST (shading); and (c), (d) precipitation (shading) and sea level pressure (contours, interval: 0.5 mb). Results for mid-Jan and mid-Apr conditions are presented in (a), (c) and (b), (d), respectively. Color shading is not used in (a), (b) at grid points where no SST anomaly has been applied in the 2 × SST experiment.

For each seasonal setting, the response of the model atmosphere to the prescribed SST anomaly in the IWP region has been obtained by subtracting the 5000-day average of the CLIMO output from the corresponding average produced by the 2 × SST run. The distributions of such differences between the 2 × SST and CLIMO experiments are shown in Figs. 8a,b for surface wind vectors (arrows) and SST (shading), and Figs. 8c,d for precipitation (shading) and sea level pressure (contours). Results for the January and April integrations are displayed in Figs. 8a,c and 8b,d, respectively. The color shading in Figs. 8a,b indicate those grid points at which anomalous SST forcing has been applied in the 2 × SST experiment. Since the near-equatorial SST anomaly in the 130°–172°E sector, as generated in the MLM experiment, appears to be a westward continuation of the zonally elongated SST forcing imposed in the DTEP region (see Figs. 1a,b), the equatorial western Pacific SST anomalies should best be treated as an integral part of the forcing that is closely associated with ENSO. We have, therefore, not prescribed any anomalous SST conditions along the entire length of the equatorial Pacific in the 2 × SST experiment. We have also excluded North Pacific SST anomalies situated east of 172°E from that experiment. A Student's t-test has been used to assess the statistical significance of the patterns displayed in Fig. 8. Most of the differences between the 2 × SST and CLIMO runs mentioned in the following discussion exceed the 95% significance level.

The patterns in Fig. 8 indicate that the typical atmospheric response to positive SST forcing is characterized by surface wind convergence [e.g., the northern Indian Ocean and the South China Sea in Jan(1) and Apr(1)] or cyclonic flows [e.g., the southern Indian Ocean in Jan(1) and the East China Sea in Apr(1)], and by negative sea level pressure and positive precipitation anomalies. Conversely, the negative SST forcing in the subtropical waters of the southwestern Pacific [Jan(1) and Apr(1)] and east of the Philippine Sea [Apr(1)] is seen to generate anticyclonic circulations, higher surface pressures, and dryer conditions. A good qualitative correspondence exists between the response signals in Fig. 8 and the difference charts of MLM versus CTRL in Fig. 7, especially during the FMAM(1)/Apr(1) period. The consistency among the findings based on these two independent methods, as described in Figs. 7–8, further enhances the credibility of both approaches. In accordance with the doubling of the amplitude of SST forcing in the 2 × SST runs, the amplitudes of the atmospheric signals in Fig. 8 are typically higher than those in Fig. 7.

A notable quantitative difference between the results in Figs. 7–8 is the much stronger cyclonic feature in the 2 × SST run (as compared to the MLM minus CTRL

pattern) associated with the warm SST and above-normal precipitation conditions in the southern Indian Ocean during Jan(1). It is, however, noteworthy that this atmospheric response is supported by the observational analysis performed by Xie et al. (2002, their Fig. 14), who pointed out that ocean upwelling induced by the cyclonic circulation serves as a negative feedback to the underlying warm SST anomaly in that region.

7. Summary and discussion

The findings presented in this study underscore the important role of the ''tropical atmospheric bridge'' in linking SST variability in the DTEP region to that in the IWP sector. As inferred from the SVD results in Figs. 1–2, the seasonal dependence of this link is characterized by the typical occurrence of maximum SST forcing in DTEP toward the end of year (0), that is, in the mature phase of the ENSO cycle, and by a 3–4 month delay of the oceanic response in IWP. The effects of the ENSO forcing are communicated to the SST field in IWP primarily by zonal displacements of the convergence centers associated with the Walker circulation in the deep Tropics, and by variations of the intensity of anticyclonic pressure cells in the subtropics of both hemispheres (Figs. 3–4). The latter atmospheric changes bear some resemblance to Rossby wave modes forced by anomalous heat sources and sinks situated near the equator, such as those generated in simple shallow-water models (Matsuno 1966; Gill 1980) and nonlinear stationary models (LNW03). The atmospheric responses to ENSO are accompanied by notable anomalies in surface wind speed, humidity, and cloud cover in the IWP region. These variations, in turn, influence the heat and radiative fluxes at the air–sea boundary, as well as the depth of the ocean mixed layer. Analysis of the heat balance of the surface ocean reveals the dominance of the contributions due to changes in latent heat fluxes and thickness of the mixed layer (Figs. 5–6), both of which exhibit a strong relationship with the anomalous surface wind speed. For the first time in our current series of studies on this subject, the incorporation of a new ocean mixed layer model with variable depth has allowed us to assess the importance of the $k\overline{Q}(1/H)'$ term, as well as the impact of the seasonally varying $\overline{H}$ on the $k(Q'_{SW} + Q'_{LW})/\overline{H}$ and $k(Q'_{LH} + Q'_{SH})/\overline{H}$ terms. Such evaluation was not feasible in our previous studies (Lau and Nath 1996, 2000, 2001), which were based on experiments using a mixed layer model with constant thickness. The advantages of a mixed layer model with variable H are demonstrated by the results in Figs. 5–6, which indicate that the SST tendencies exhibit a strong dependence on changes in H' and $\overline{H}$.

In much of the IWP region at the end of year (0), the total SST tendencies induced by various atmospheric forcing mechanisms have the same polarity as that of the local SST anomalies. Such cooperative interaction between the atmospheric driving and the SST field sustains the development of the SST anomalies through the northern spring of year(1). The difference charts between the output from the MLM and CTRL experiments (Fig. 7), as well as the GCM responses to prescribed SST forcing in the IWP region (Fig. 8), indicate that the feedback of the SST anomalies on the overlying atmospheric circulation is an important facet of the air–sea coupling in the IWP region. Comparison between the atmospheric anomaly patterns simulated in the MLM experiment (Fig. 3) and the results in Figs. 7–8 suggests that several prominent features in the former charts, such as intensification of the rainbelt over the east Asian coast and the eastward migration of the anomalous subtropical anticyclones during the northern spring of year(1), can be attributed to feedbacks of the SST changes on the atmospheric environment.

The empirical studies of Curtis and Hastenrath (1995), Enfield and Mayer (1997), and Klein et al. (1999) have provided evidence on another atmospheric bridge connecting the DTEP region with the tropical Atlantic. The MLM and CTRL experiments conducted for the present study are suited for investigating the ENSO-related variability of the coupled system in the Atlantic sector. Various aspects of the atmosphere–ocean interaction in that region could also be examined by applying some of the analysis techniques developed here.

In this study, we have focused our attention on composite fields that were obtained by averaging the data for several ENSO events and for multiple model realizations of each event. Preliminary statistics presented in LNW03 (see their Fig. 4) indicate considerable interevent and intersample variability among the model signals. Further diagnoses are needed to determine the origin of these sampling fluctuations, and to investigate the nonlinear aspects the atmosphere–ocean variability in the IWP sector with regards to the polarity and strength of the forcing. Of particular interest are the dependencies of the intersample variations and nonlinear behavior on the specific characteristics of each ENSO event, and on the atmosphere–ocean state in the onset stage of the events. Resolution of these complex issues would advance our understanding of the predictability of the coupled system in the IWP region in the presence of ENSO forcing. Such investigations would be facilitated by the availability of a relatively large number of individual samples (16 and 8 for the MLM and CTRL experiments, respectively).

It should be stressed that only a subset of oceanic processes has been incorporated in the simple mixed layer model used in this study. This tool is evidently not adequate for representing the air–sea interaction in locations where oceanic changes are strongly influenced by various dynamical mechanisms, such as advection by ocean currents, upwelling, Ekman effects, and propagation of modal structures. The importance of the latter processes in the variability of the coupled system in the Indian Ocean, and particularly in the generation of east–

west contrasts in the SST field along the equator in that basin, has been noted by Webster et al. (1999), Saji et al. (1999), Murtugudde et al. (2000), and Xie et al. (2002), among others. Further investigations with fully coupled GCMs are needed to assess the individual contributions by surface flux forcing and ocean dynamics to, as well as the relative roles of remote ENSO forcing and internal atmosphere–ocean interactions in, the recurrent modes of atmosphere–ocean variability in the tropical Indian and Atlantic Oceans.

Acknowledgments. We would like to thank John Lanzante for undertaking the laborious tasks of executing the MLM and CTRL runs examined in this study; Mike Alexander and Jamie Scott for software support for coupling the oceanic mixed layer model to the atmospheric GCM; various GFDL colleagues for providing computer resources for the model integrations; and Mike Alexander, Steve Klein, John Lanzante, and Bill Stern for insightful comments on earlier versions of this manuscript. The constructive suggestions by the two official reviewers have led to substantial clarification of some of the issues addressed in this article.

REFERENCES

Alexander, M. A., C. Deser, and J. D. Scott, 2000: Processes that influence sea surface temperature and ocean mixed layer depth variability in a coupled model. *J. Geophys. Res.,* **105,** 16 823–16 842.

——, I. Bladé, M. Newman, J. R. Lanzante, N.-C. Lau, and J. D. Scott, 2002: The atmospheric bridge: The influence of ENSO teleconnections on air–sea interaction over the global oceans. *J. Climate,* **15,** 2205–2231.

Allan, R. J., and Coauthors, 2001: Is there an Indian Ocean dipole, and is it independent of the El Niño–Southern Oscillation? *CLIVAR Exchanges,* **6,** 18–22.

Baquero-Bernal, A., M. Latif, and S. Legutke, 2002: On the dipolelike variability of sea surface temperature in the tropical Indian Ocean. *J. Climate,* **15,** 1358–1368.

Barnett, T. P., 1985: Variations in near-global sea level pressure. *J. Atmos. Sci.,* **42,** 478–501.

Behera, S. K., P. S. Salvekar, and T. Yamagata, 2000: Simulation of interannual SST variability in the tropical Indian Ocean. *J. Climate,* **13,** 3487–3499.

Bretherton, C. S., C. Smith, and J. M. Wallace, 1992: An intercomparison of methods for finding coupled patterns in climate data. *J. Climate,* **5,** 541–560.

Broccoli, A. J., and S. Manabe, 1992: The effects of orography on midlatitude Northern Hemisphere dry climates. *J. Climate,* **5,** 1181–1201.

Chang, C.-P., Y. Zhang, and T. Li, 2000: Interannual and interdecadal variations of the East Asian summer monsoon and tropical Pacific SSTs. Part I: Roles of the subtropical ridge. *J. Climate,* **13,** 4310–4325.

Curtis, S., and S. Hastenrath, 1995: Forcing of anomalous sea surface temperature evolution in the tropical Atlantic during Pacific warm events. *J. Geophys. Res.,* **100,** 15 835–15 847.

Enfield, D. B., and D. A. Mayer, 1997: Tropical Atlantic sea surface temperature variability and its relation to El Niño–Southern Oscillation. *J. Geophys. Res.,* **102,** 929–945.

——, and A. M. Mestas-Nuñez, 1999: Multiscale variabilities in global sea surface temperatures and their relationships with tropospheric climate patterns. *J. Climate,* **12,** 2719–2733.

Gaspar, P., 1988: Modelling the seasonal cycle of the upper ocean. *J. Phys. Oceanogr.,* **18,** 161–180.

Gill, A. E., 1980: Some simple solutions for heat-induced tropical circulation. *Quart. J. Roy. Meteor. Soc.,* **106,** 447–462.

Gordon, C. T., and W. F. Stern, 1982: A description of the GFDL global spectral model. *Mon. Wea. Rev.,* **110,** 625–644.

Harrison, D. E., and N. K. Larkin, 1998: El Niño–Southern Oscillation sea surface temperature and wind anomalies, 1946–1993. *Rev. Geophys.,* **36,** 353–399.

Hastenrath, S., 2002: Dipoles, temperature gradients, and tropical climate anomalies. *Bull. Amer. Meteor. Soc.,* **83,** 735–738.

——, A. Nicklis, and L. Greischar, 1993: Atmospheric–hydrospheric mechanisms of climate anomalies in the western equatorial Indian Ocean. *J. Geophys. Res.,* **98,** 20 219–20 235.

Hoerling, M. P., A. Kumar, and M. Zhong, 1997: El Niño, La Niña, and the nonlinearity of their teleconnections. *J. Climate,* **10,** 1769–1786.

Kawamura, R., 1994: A rotated EOF analysis of global sea surface temperature variability with interannual and interdecadal scales. *J. Phys. Oceanogr.,* **24,** 707–715.

——, T. Matsuura, and I. Satoshi, 2001a: Role of equatorially asymmetric sea surface temperature anomalies in the Indian Ocean in the Asian summer monsoon and El Niño–Southern Oscillation coupling. *J. Geophys. Res.,* **106,** 4681–4693.

——, ——, and ——, 2001b: Interannual atmosphere–ocean variations in the tropical western North Pacific relevant to the Asian summer monsoon–ENSO coupling. *J. Meteor. Soc. Japan,* **79,** 883–898.

Kiladis, G. N., and H. F. Diaz, 1989: Global climatic anomalies associated with extremes in the Southern Oscillation. *J. Climate,* **2,** 1069–1090.

Klein, S. A., B. J. Soden, and N.-C. Lau, 1999: Remote sea surface temperature variations during ENSO: Evidence for a tropical atmospheric bridge. *J. Climate,* **12,** 917–932.

Lanzante, J. R., 1996: Lag relationships involving tropical sea surface temperatures. *J. Climate,* **9,** 2568–2578.

Larkin, N. K., and D. E. Harrison, 2001: Tropical Pacific ENSO cold events, 1946–95: SST, SLP, and surface wind composite anomalies. *J. Climate,* **14,** 3904–3931.

——, and ——, 2002: ENSO warm (El Niño) and cold (La Niña) event life cycles: Ocean surface anomaly patterns, their symmetries, asymmetries, and implications. *J. Climate,* **15,** 1118–1140.

Lau, K.-M., and H. T. Wu, 2001: Principal modes of rainfall-SST variability of the Asian summer monsoon: A reassessment of the monsoon–ENSO relationship. *J. Climate,* **14,** 2880–2895.

Lau, N.-C., and M. J. Nath, 1996: The role of the ''atmospheric bridge'' in linking tropical Pacific ENSO events to extratropical SST anomalies. *J. Climate,* **9,** 2036–2057.

——, and ——, 2000: Impact of ENSO on the variability of the Asian–Australian monsoons as simulated in GCM experiments. *J. Climate,* **13,** 4287–4309.

——, and ——, 2001: Impact of ENSO on SST variability in the North Pacific and North Atlantic: Seasonal dependence and role of extratropical sea–air coupling. *J. Climate,* **14,** 2846–2866.

——, ——, and H. Wang, 2003: Simulations by a GFDL GCM of ENSO-related variability of the coupled atmosphere–ocean system in East Asian monsoon region. *East Asian Monsoon,* C.-P. Chang, Ed., World Scientific Series on Meteorology of East Asia, Vol. 2, World Scientific, in press.

Luo, J.-J., and T. Yamagata, 2001: Long-term El Niño–Southern Oscillation (ENSO)-like variation with special emphasis on the South Pacific. *J. Geophys. Res.,* **106,** 22 211–22 227.

Manabe, S., R. J. Stouffer, M. J. Spelman, and K. Bryan, 1991: Transient responses of coupled ocean–atmosphere model to gradual changes of atmospheric CO_2. Part I: Annual mean responses. *J. Climate,* **4,** 785–818.

Matsuno, T., 1966: Quasi-geostrophic motions in the equatorial area. *J. Meteor. Soc. Japan,* **44,** 25–43.

McBride, J. L., and N. Nicholls, 1983: Seasonal relationships between

Australian rainfall and the Southern Oscillation. *Mon. Wea. Rev.,* **111,** 1998–2004.

Mooley, D. A., and B. Parthasarathy, 1983: Indian summer monsoon and El Niño. *Pure Appl. Geophys.,* **121,** 339–352.

Murtugudde, R., and A. J. Busalacchi, 1999: Interannual variability of the dynamics and thermodynamics of the tropical Indian Ocean. *J. Climate,* **12,** 2300–2326.

——, J. P. McCreary, and A. J. Busalacchi, 2000: Oceanic processes associated with anomalous events in the Indian Ocean with relevance to 1997–1998. *J. Geophys. Res.,* **105,** 3295–3306.

Nicholson, S. E., 1997: An analysis of the ENSO signal in the tropical Atlantic and western Indian Oceans. *Int. J. Climatol.,* **17,** 345–375.

Nitta, T., and S. Yamada, 1989: Recent warming of tropical sea surface temperature and its relationship to the Northern Hemisphere circulation. *J. Meteor. Soc. Japan,* **67,** 375–383.

Pan, Y. H., and A. H. Oort, 1983: Global climate variations connected with sea surface temperature anomalies in the eastern equatorial Pacific Ocean for the 1958–73 period. *Mon. Wea. Rev.,* **111,** 1244–1258.

——, and ——, 1990: Correlation analyses between sea surface temperature anomalies in the eastern equatorial Pacific and the world ocean. *Climate Dyn.,* **4,** 191–205.

Rao, S. A., S. K. Behera, Y. Masumoto, and T. Yamagata, 2002: Interannual subsurface variability in the tropical Indian Ocean with a special emphasis on the Indian Ocean dipole. *Deep-Sea Res.,* **49B,** 1549–1572.

Rasmusson, E. M., and T. H. Carpenter, 1983: The relationship between the eastern Pacific sea surface temperature and rainfall over India and Sri Lanka. *Mon. Wea. Rev.,* **111,** 517–528.

Saji, N. H., B. N. Goswami, P. N. Vinayachandran, and T. Yamagata, 1999: A dipole mode in the tropical Indian Ocean. *Nature,* **401,** 360–363.

Slingo, J. M., and H. Annamalai, 2000: 1997: The El Niño of the century and the response of the Indian summer monsoon. *Mon. Wea. Rev.,* **128,** 1778–1797.

Smith, T. M., R. W. Reynolds, R. E. Livezey, and D. C. Stokes, 1996: Reconstruction of historical sea surface temperatures using empirical orthogonal functions. *J. Climate,* **9,** 1403–1420.

Tourre, Y. M., and W. B. White, 1995: ENSO signals in global upper-ocean temperature. *J. Phys. Oceanogr.,* **25,** 1317–1332.

Trenberth, K. E., 1997: The definition of El Niño. *Bull. Amer. Meteor. Soc.,* **78,** 2771–2777.

Venzke, S., M. Latif, and A. Villwock, 2000: The coupled GCM ECHO-2. Part II: Indian Ocean response to ENSO. *J. Climate,* **13,** 1371–1383.

Wang, B., R. Wu, and X. Fu, 2000: Pacific–East Asian teleconnection: How does ENSO affect East Asian climate? *J. Climate,* **13,** 1517–1536.

Webster, P. J., A. M. Moore, J. P. Loschnigg, and R. R. Leben, 1999: Coupled ocean–atmosphere dynamics in the Indian Ocean during 1997–98. *Nature,* **401,** 356–360.

Wetherald, R. T., and S. Manabe, 1988: Cloud feedback processes in a general circulation model. *J. Atmos. Sci.,* **45,** 1397–1415.

Xie, S.-P., H. Annamalai, F. A. Schott, and J. P. McCreary, 2002: Structure and mechanisms of South Indian Ocean climate variability. *J. Climate,* **15,** 864–878.

Yasunari, T., 1985: Zonally propagating modes of the global east–west circulation associated with the Southern Oscillation. *J. Meteor. Soc. Japan,* **63,** 1013–1029.

——, 1987: Global structure of the El Niño/Southern Oscillation. Part II. Time evolution. *J. Meteor. Soc. Japan,* **65,** 81–102.

Yu, L.-S., and M. M. Reinecker, 1999: Mechanisms for the Indian Ocean warming during the 1997–98 El Niño. *Geophys. Res. Lett.,* **26,** 735–738.

Zhang, R., A. Sumi, and M. Kimoto, 1996: Impact of El Niño on the east Asian monsoon: A diagnostic study of the '86/87 and '91/92 events. *J. Meteor. Soc. Japan,* **74,** 49–62.

Zhang, Y., J. M. Wallace, and D. S. Battisti, 1997: ENSO-like interdecadal variability: 1900–93. *J. Climate,* **10,** 1004–1020.